electronics

MDPI

Article

In-Orbit Calibration of Phased Array Antennas Using GNSS Carrier-Phase Measurements

Qifei Du [1,2], Zijie Wang [1,2,*], Yueqiang Sun [1,2], Xiangguang Meng [1,2], Junming Xia [1,2], Dongwei Wang [1,2] and Hao Zhang [1]

[1] Key Laboratory of Science and Technology on Space Environment Situational Awareness, National Space Science Center, Beijing 100190, China; dqf@nssc.ac.cn (Q.D.); syq@nssc.ac.cn (Y.S.); xgmeng@nssc.ac.cn (X.M.); xiajunming@nssc.ac.cn (J.X.); wangdongwei@nssc.ac.cn (D.W.); zhanghao@nssc.ac.cn (H.Z.)
[2] University of Chinese Academy of Sciences, Beijing 100190, China
* Correspondence: wangzijie251@mails.ucas.ac.cn

Abstract

This paper proposes a passive in-orbit calibration method for phased array antennas using GNSS carrier-phase measurements. By performing synchronous observation and exploiting the short-baseline property between the positioning antenna and array elements, the first differencing operation eliminates space propagation errors and clock biases. By further utilizing receiver channel consistency, the second differencing operation cancels out the receiver channel errors, thereby extracting the relative receive-chain phase error of the element under test. Under typical operating conditions, the calibration accuracy can reach an RMS error of approximately 3.02 mm, corresponding to a phase accuracy of 5.72° in the GPS L1 band. This accuracy is close to the 5.625° minimum phase step of a 6-bit digital phase shifter, and can be further improved under higher C/N_0 and well-controlled residual error conditions. Without requiring a dedicated GNSS band excitation signal, this method avoids co-frequency self-interference with the positioning antenna, which provides an auxiliary approach for in-orbit calibration of phased array receive chains.

Keywords: phased array antennas; in-orbit calibration; GNSS carrier-phase; co-frequency self-interference

1. Introduction

Spaceborne phased array antennas operating in the GNSS band have become important payloads on LEO satellite platforms because of their millisecond-level beam agility, multibeam spatial multiplexing capability, and high gain. However, cyclic temperature variation, high-energy particle radiation, and component aging in the in-orbit environment can cause drift in the amplitude and phase characteristics of T/R channels, which degrades system reliability [1–4]. To compensate for the resulting distortion, phased array antennas must be calibrated periodically.

A common calibration approach is the rotating element electric field vector (REV) method, which analyzes amplitude and phase errors by sequentially rotating the phase of a single channel and measuring the resultant power variation. This method has low hardware requirements, but it suffers from long calibration time, weak power fluctuation of a single element, and poor SNR in far-field observation [5–7]. Another method is orthogonal coding, in which each T/R channel is assigned an orthogonal code sequence. This method allows all elements to be activated in parallel and greatly improves the calibration speed,

Check for updates

Academic Editor: Massimo Donelli

Received: 2 May 2026
Revised: 9 June 2026
Accepted: 18 June 2026
Published: 22 June 2026

Copyright: © 2026 by the authors. Licensee MDPI, Basel, Switzerland. This article is an open access article distributed under the terms and conditions of the Creative Commons Attribution (CC BY) license.

but it also increases the complexity of the baseband hardware [8–10]. These methods are therefore not ideal for LEO satellite platforms with limited onboard resources.

From the viewpoint of system architecture, calibration methods can be divided into internal calibration and external calibration, depending on whether the calibration loop includes the antenna aperture and free-space [11,12]. Internal calibration relies on the internal RF coupling network. It enables high-frequency closed-loop monitoring without being affected by the external environment, but it still leaves residual calibration errors [13,14]. External calibration uses an external radiation source to perform an end-to-end measurement. It captures the combined effects of internal hardware and the external environment, and therefore reflects system characteristics more completely [15].

As shown in Figure 1, conventional external calibration methods usually require an excitation source. During in-orbit calibration, the excitation source radiates a reference signal toward the antenna aperture, and the corresponding calibration quantities are obtained by measuring and comparing the phase responses of different receive channels. For a spaceborne phased array operating in the GNSS band, the excitation source must operate within or near the GNSS frequency band to match the frequency. Therefore, the excitation signal can be received not only by the phased array elements, but also by the positioning antenna. This signal may then cause co-frequency interference with the GNSS satellite signals used for orbit determination. Such self-interference can degrade the positioning function performance and pose a serious risk to platform safety.

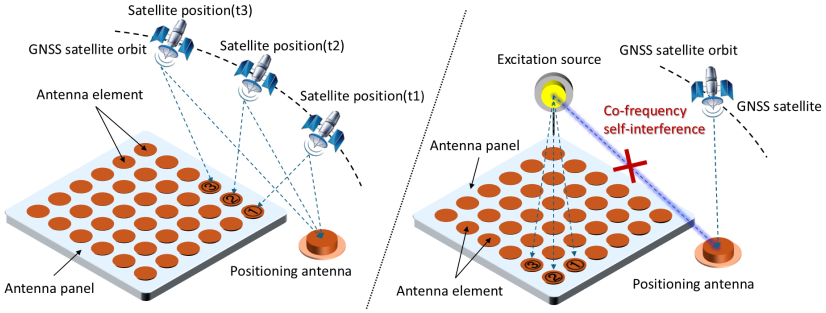


Figure 1. Comparison between the proposed method and the conventional external calibration method. The proposed method uses visible GNSS satellites as passive radiation sources, whereas the conventional method relies on an onboard GNSS band excitation source, which may introduce co-frequency self-interference to the positioning antenna.

To address this issue, passive calibration based on signals of opportunity, namely GNSS signals, is considered. Anantharamu et al. proposed an array calibration algorithm based on GNSS signals and orthogonal projection, and verified its feasibility in beamforming and direction-of-arrival (DoA) applications using hardware simulation and real GPS signals [16]. Schuss et al. proposed the SatCal method, which uses echoes generated when satellites are illuminated to calibrate large-scale phased arrays, thus avoiding complex near-field testing [17,18]. Wang et al. proposed a method that uses spaceborne measurements to retrieve the gain patterns of the receiving antennas on GPS and CYGNSS satellites, further demonstrating the feasibility of phased array calibration based on GNSS observations [19].

Recent studies on GNSS processing and sensor array calibration also support the feasibility of low-overhead, reference-based measurement strategies. Zhang et al. improved weak GNSS signal acquisition using an SFFT-based fast acquisition algorithm [20], while Li et al. emphasized the role of robust time synchronization in GNSS/IMU integrated navigation [21]. For sensor arrays, Zhang et al. demonstrated that internal-reference calibration with explicit error modeling can improve calibration robustness [22]. These works motivate the use of existing GNSS signals and well-defined error models for auxiliary in-orbit calibration.

Inspired by these studies, this article investigates an auxiliary in-orbit calibration method for spaceborne phased array antennas using visible GNSS satellites and double-differenced carrier-phase observations. The objective of this method is to calibrate the relative receive-chain phase of the selected array element with respect to that of the reference element, rather than to perform complete far-field array calibration. Factors required for full-aperture calibration, such as phase center variation and scan-angle dependence, are assumed to have been characterized through pre-launch ground calibration and are treated in this work as predetermined parameters or residual error sources.

Under the short-baseline synchronous observation condition and the receiver channel consistency assumption, the double-differencing process can suppress the effects of common propagation errors, clock-related terms, and receiver channel contributions. The resulting phase estimate can then be used as an auxiliary calibration quantity and compared with the pre-launch calibrated data to evaluate and correct the relative receive-chain phase deviation of the selected array element.

The main contributions of this work are summarized as follows. First, a passive in-orbit calibration framework using visible GNSS satellites as signals of opportunity is proposed, avoiding the need for a GNSS band excitation source and thereby reducing the risk of co-frequency self-interference with the positioning antenna. Second, a double-differenced carrier-phase formulation is developed to isolate the relative receive-chain phase error of a selected element with respect to a reference element. Third, a stochastic link-budget model and a residual error budget are introduced to evaluate the practical calibration accuracy under realistic operating conditions, demonstrating the potential of the proposed method for in-orbit phase-drift monitoring and auxiliary receive-chain calibration of LEO phased arrays.

2. Materials and Methods

Consider a 6×6 phased array antenna installed on a LEO satellite. A satellite body-fixed coordinate system O-xyz is established, with the center of element 1 taken as the origin. The positions of the other 35 elements are defined relative to element 1. The position vector of the n-th element ($n = 1, 2, \ldots, 36$) is written as $\mathbf{r}_n = [x_n, y_n, z_n]^T$

The GNSS satellite used as the radiation source is approximately 20,000 km away from the LEO satellite. This distance is much larger than the aperture size of the phased array. Therefore, the electromagnetic wavefront across the array can be treated as an ideal plane wave.

2.1. GNSS Signal Reception

Assume that the GNSS signal arrives from the direction (θ, φ), where θ is the elevation angle, φ is the azimuth angle, λ is the carrier wavelength, and the unit vector pointing toward the signal source is $\mathbf{u}(\theta, \varphi) = [\cos\theta\cos\varphi,\ \cos\theta\sin\varphi,\ \sin\theta]^T$.

The electromagnetic wavefront reaches the n-th element with a time delay or advance relative to the reference element. The path difference Δd_n is the projection of the position vector onto the propagation direction. Let c denote the speed of light in vacuum. As shown in Figure 2, the time delay t_n is

$$t_n(\theta, \varphi) = \frac{\Delta d_n}{c} = -\frac{\mathbf{r}_n^T \mathbf{u}(\theta, \varphi)}{c} \tag{1}$$

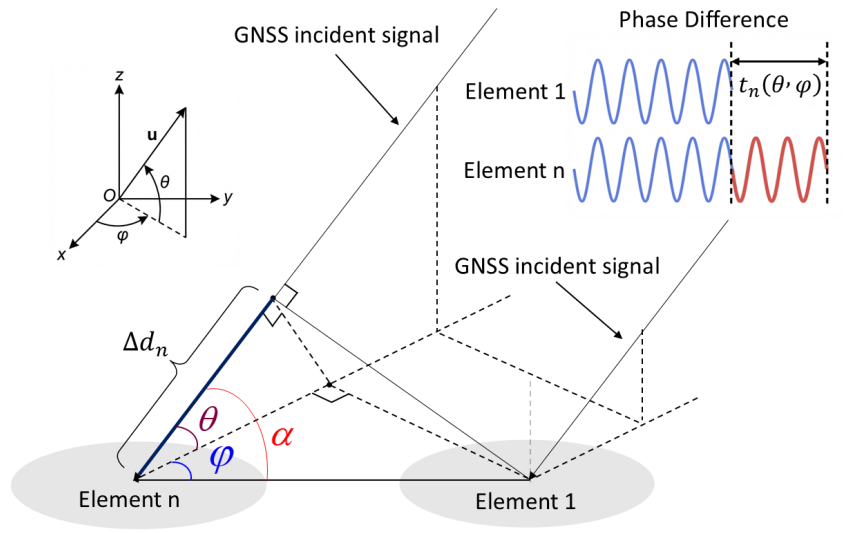


Figure 2. Geometric relationship between antenna elements and the incident GNSS signal.

Since the bandwidth of the GNSS signal is much smaller than the L-band carrier frequency, the signal envelope can be treated as unchanged. The inter-element delay effect can be simplified to a carrier phase shift [23]. The steering vector of the nth element and the array manifold vector can be written as

$$a_n(\theta, \varphi) = \exp(-j\omega_0 \tau_n) = \exp\left(j\frac{2\pi}{\lambda}\mathbf{r}_n^T\mathbf{u}(\theta, \varphi)\right) \tag{2}$$

$$\mathbf{a}(\theta, \varphi) = \begin{bmatrix} 1 \\ \exp\left(j\frac{2\pi}{\lambda}\mathbf{r}_2^T\mathbf{u}(\theta, \varphi)\right) \\ \vdots \\ \exp\left(j\frac{2\pi}{\lambda}\mathbf{r}_N^T\mathbf{u}(\theta, \varphi)\right) \end{bmatrix} \in \mathbb{C}^{N\times 1} \tag{3}$$

Mutual coupling is not explicitly included in (3). The proposed method aims to estimate the relative receive-chain phase of the selected array element with respect to the reference element, rather than to perform complete full-aperture far-field array calibration. Moreover, the phased array operates in a receive-only mode during the proposed calibration procedure; no array element is actively excited or used for signal transmission.

In calibration mode, as shown in Figure 3, the microwave switch matrix ensures that only one array element is selected at a given time, while all the remaining elements are terminated with matched loads. This configuration can effectively suppress signal leakage through unselected receive channels and reduce coupling contributions caused by load reflections. Nevertheless, the passive scattering and embedded element responses are not assumed to vanish. These effects are regarded as intrinsic aperture characteristics of the array and should be characterized during pre-launch ground calibration. Therefore, in this work, they are treated as predetermined parameters or residual error sources, rather than quantities directly solved by the proposed double-differenced carrier-phase method.

After the signal is received by an array element, it passes through RF components such as the low-noise amplifier, power divider, digital phase shifter, and transmission cable. Differences among these components introduce unknown amplitude and phase errors.

First, we need to analyze the impact weights of amplitude and phase errors on antenna performance. For this purpose, a numerical simulation is conducted by introducing random amplitude and phase errors into the array excitation and evaluating the resulting

degradation of the radiation characteristics. The simulation parameters and evaluation metrics are listed in Table 1 and Table 2, respectively.

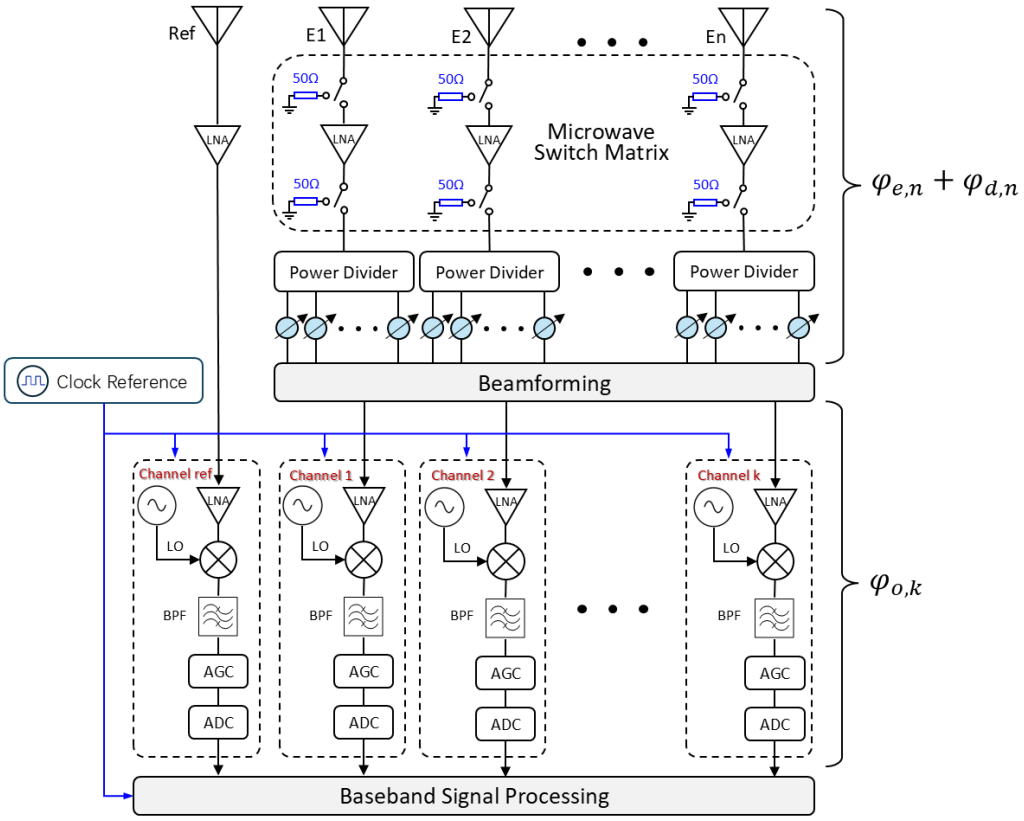


Figure 3. Schematic diagram of the system architecture: antenna elements, microwave switch matrix, beamforming network, and receiver channels.

Table 1. Simulation parameter settings.

Parameter	Description	Value
Array configuration	Uniform planar array located on the x-y plane	6×6 uniform planar array
Normalized wavelength	Normalized wavelength modeling is adopted	1
Element spacing	Half-wavelength spacing	0.5λ (x and y directions)
Desired beam direction	The array broadside direction	$\theta_0 = 0^\circ$, $\phi_0 = 0^\circ$
Principal-cut scanning range	Angular range for the principal-cut pattern	-60° to 60°
Principal-cut scanning step	Angular interval between adjacent scanning points	0.05°
Principal-cut azimuth angle	The $\phi = 0^\circ$ azimuth cut is observed	$\phi = 0^\circ$
Amplitude error	Uniform random amplitude errors	± 2, ± 2.5, ± 3, ± 3.5 dB
Phase error	Uniform random phase errors	$\pm 20^\circ$, $\pm 30^\circ$, $\pm 40^\circ$, $\pm 50^\circ$
Number of Monte Carlo trials	Used to calculate the mean and standard deviation	200
Two-dimensional u-v search range	Search range for the two-dimensional main-beam peak	$\lvert u\rvert, \lvert v\rvert \leq \sin(60^\circ)$
Two-dimensional u-v search step	A smaller step improves pointing-search resolution	0.02

The amplitude and phase errors are modeled as independent uniformly distributed random variables. For a given amplitude error bound A_{err}, the amplitude error of each element follows $\Delta G_n \sim \mathcal{U}(-A_{\mathrm{err}}, A_{\mathrm{err}})$ in dB. For a given phase error bound P_{err}, the phase error of each element follows $\Delta\phi_n \sim \mathcal{U}(-P_{\mathrm{err}}, P_{\mathrm{err}})$ in degrees.

Table 2. Evaluation metrics and calculation formulas.

Metric	Calculation Formula
Normalized radiation pattern	$P_{\mathrm{dB}}(\theta) = 10\log_{10}\left(\frac{P(\theta)}{\max P(\theta)}\right)$
Synthesis efficiency	$\eta = \frac{\left\lvert\sum_{n=1}^{N} e^{jk(u_0x_n+v_0y_n)}a_n\right\rvert^2}{N\sum_{n=1}^{N}\lvert a_n\rvert^2}$
Two-dimensional pointing error	$\Delta\alpha = \cos^{-1}(u_pu_0 + v_pv_0 + w_pw_0)$
3-dB beamwidth	$\mathrm{HPBW} = \theta_R - \theta_L$
Peak sidelobe level	$\mathrm{PSL} = 10\log_{10}\left(\frac{\max P_{\mathrm{sidelobe}}}{P_{\max}}\right)$
Monte Carlo mean value	$\bar{x} = \frac{1}{M}\sum_{m=1}^{M} x_m$
Monte Carlo standard deviation	$\sigma = \sqrt{\frac{1}{M-1}\sum_{m=1}^{M}(x_m - \bar{x})^2}$

Here, N denotes the total number of array elements, M denotes the number of Monte Carlo trials, a_n denotes the actual excitation of the n-th element, (u_0, v_0, w_0) denotes the unit direction vector of the desired beam direction, and (u_p, v_p, w_p) denotes the unit direction vector of the actual main-beam peak.

Figure 4 compares the principal-cut radiation patterns under random amplitude and phase errors. It can be observed that amplitude errors have only a limited influence on the main beam, and their main effect is reflected in slight sidelobe fluctuations. In contrast, phase errors cause more evident pattern degradation, including main-beam distortion, sidelobe deterioration, and beam pointing deviation.

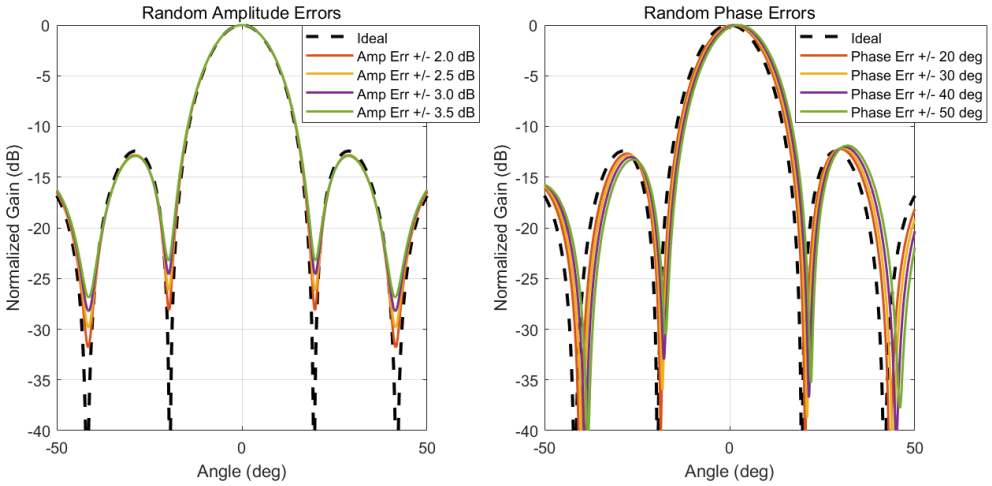


Figure 4. Array pattern under the influence of random amplitude and phase errors.

To further quantify the different effects of the two error types, Monte Carlo simulations are performed, and the statistical trends of several array-performance metrics are shown in Figure 5.

The results show that the synthesis efficiency decreases only slightly under increasing amplitude errors, whereas it decreases much more significantly under increasing phase errors. A similar tendency is observed for the two-dimensional pointing error: amplitude errors introduce almost no beam pointing deviation, while phase errors lead to a continuously increasing pointing error. The 3-dB beamwidth remains relatively stable in both cases, indicating that the main-lobe width is not the most sensitive metric in this simulation. However, the peak sidelobe level deteriorates more evidently under phase errors than under amplitude errors. These results provide quantitative evidence that phase errors dominate the degradation of synthesis efficiency, pointing accuracy, and sidelobe performance.

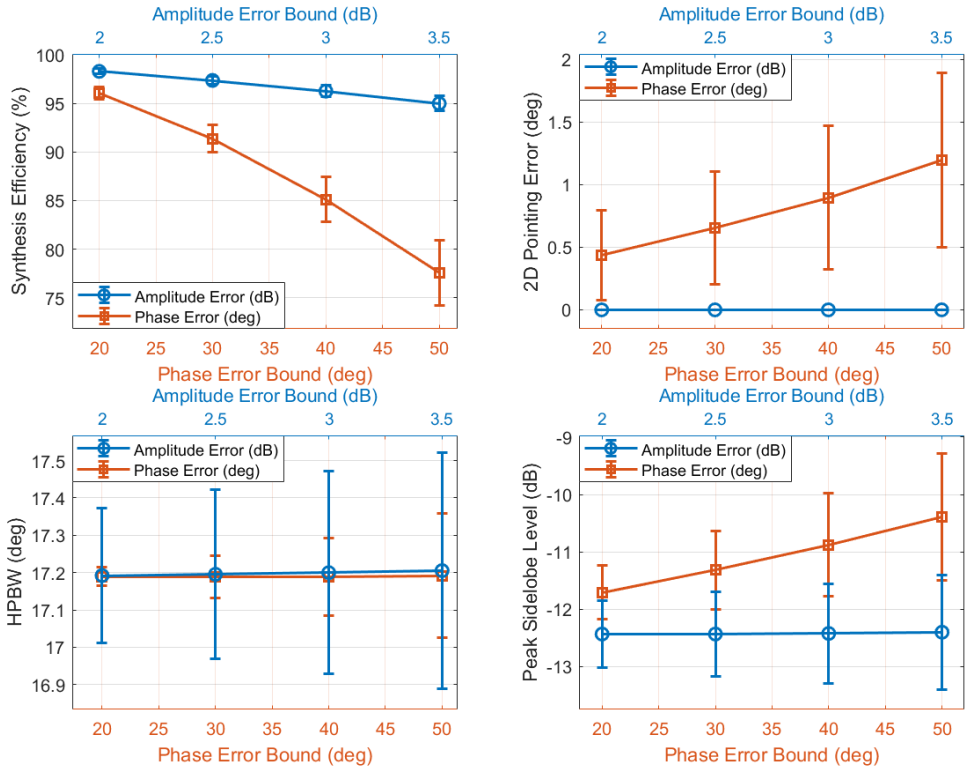


Figure 5. Trend comparison with increasing random amplitude and phase errors. The **upper** and **lower** x-axes represent amplitude error bounds in dB and phase error bounds in degrees, respectively; they are used for trend comparison and do not imply dimensional equivalence.

Therefore, in the present system, the array synthesis efficiency and pointing accuracy are mainly determined by phase errors, while amplitude errors are less critical. Since Gao et al. have already proposed an in-orbit amplitude calibration method for phased array antennas [24], the present work focuses on phase calibration.

The 6×6 uniform planar array adopted in the simulation can be regarded as a representative moderate-scale configuration. This configuration contains a sufficient number of elements to exhibit typical two-dimensional array characteristics, while still allowing clear radiation pattern visualization and statistically stable Monte Carlo analysis.

In addition, the proposed framework can be extended to larger-scale arrays. Since the array elements are sequentially selected, the calibration process essentially estimates the relative receive-chain phase of each selected element with respect to the receive-chain phase of the reference element. Therefore, when the method is extended to larger arrays, the main cost is an approximately linear increase in calibration time.

It should be noted that if all elements can be calibrated within the observation interval of one visible GNSS satellite, the same reference element can be used throughout the entire procedure. If the array is too large to complete the calibration of all elements within the available observation interval of a single GNSS satellite, the array can be divided into multiple subsets and calibrated sequentially. For example, elements 1–20 may be calibrated using one GNSS satellite in the first interval. After switching to another GNSS satellite, element 1 should be re-observed first, and the calibration can then continue for elements 21–40.

A signal reception model with channel errors is established by defining the complex gain of the nth channel as $g_n = \alpha_n \exp(j\varphi_{e,n})$ [25], where α_n is the amplitude gain error and $\varphi_{e,n}$ is the additional phase delay introduced by the antenna, cable, and RF circuitry. The total phase delay of the nth element is written as

$$\varphi_n = \varphi_{d,n} + \varphi_{e,n} + \varphi_{o,k} \tag{4}$$

where $\varphi_{d,n}$ is the digital phase shifter setting, which is known and is set to zero during calibration, and $\varphi_{o,k}$ is the receiver channel delay (detailed in Section 3). Let $s(t)$ denote the complex envelope of the signal. Then the received signal at the nth element and the array output are

$$\begin{aligned} x_n(t) &= g_n s(t) \exp(j\omega_0 t) a_n(\theta, \varphi) \\ &= \alpha_n \exp(j(\varphi_{d,n} + \varphi_{e,n})) s(t) \exp(j\omega_0 t) \exp\left(j\frac{2\pi}{\lambda}\mathbf{r}_n^T \mathbf{u}(\theta, \varphi)\right) \end{aligned} \tag{5}$$

$$\mathbf{x}(t) = \mathbf{\Gamma}\mathbf{a}(\theta, \varphi) s(t) e^{j\omega_0 t} \tag{6}$$

where $\mathbf{\Gamma} = \mathrm{diag}\{g_1, g_2, \ldots, g_N\}$ is the array error matrix. The goal of calibration is to estimate the phase terms in $\mathbf{\Gamma}$, namely the relative phase delay of element n with respect to element 1, defined as $\Delta\varphi_{e,n} = \varphi_{e,n} - \varphi_{e,1}$.

2.2. Carrier-Phase Observation Equations

To estimate the unknown phase $\varphi_{e,n}$, GNSS carrier-phase measurement is adopted. The system includes a positioning antenna and the phased array elements under testing. The positioning antenna is an independent hemispherical-beam antenna used for precise orbit determination of the LEO satellite. Its phase center is known and stable, so it is used as the calibration reference.

For the same GNSS satellite, the carrier-phase observation of the positioning antenna is denoted by Φ_r, and that of the nth phased array element is denoted by Φ_n. The observation equation for the positioning antenna is

$$\Phi_r = \varphi_r + \frac{2\pi}{\lambda}(R_r + \lambda N_r + \Psi_{com}) + \varepsilon_r \tag{7}$$

where φ_r is the phase delay of the positioning antenna and its RF front end, R_r is the geometric distance from the positioning antenna phase center to the transmitting antenna phase center of the GNSS satellite, N_r is the carrier-phase integer ambiguity, Ψ_{com} is the combined error term including ionospheric delay, tropospheric delay and receiver clock bias, and ε_r is the thermal noise error.

In calibration mode, the microwave switch matrix selects only the nth phased array element for reception, while all other elements are terminated with matched loads. At the same time, the digital phase shifter of that element is set to zero. After continuous tracking for a certain period, the carrier-phase observation of the selected element is

$$\Phi_n = \varphi_n + \frac{2\pi}{\lambda}(R_n + \lambda N_n + \Psi_{com}) + \varepsilon_n \tag{8}$$

where φ_n is the total phase delay of the nth channel, R_n is the geometric distance from the phase center of the nth phased array element to the GNSS transmitting antenna phase center, N_n is the integer ambiguity of that channel, and ε_n is the thermal noise error.

2.3. Double-Difference Calibration Principle

A single observation equation cannot separate the total phase delay φ_n. Therefore, a first differencing operation is performed by exploiting spatial correlation. At the same time, the carrier-phase observation of element n is differenced with that of the positioning antenna:

$$\Delta\Phi_n = \Phi_n - \Phi_r = (\varphi_n - \varphi_r) + \frac{2\pi}{\lambda}[(R_n - R_r) + \lambda(N_n - N_r)] + (\varepsilon_n - \varepsilon_r) \tag{9}$$

The positioning antenna and the phased array are physically close to each other. They also share the same high-stability clock source and are sampled synchronously. From the viewpoint of the GNSS satellite, two signal propagation paths are nearly identical. Under this short-baseline and synchronous observation condition, Ψ_{com} acts as a common-mode error and is therefore canceled directly.

If the satellite attitude and the installation position of the positioning antenna are known, the path difference between the positioning antenna and element n, denoted by $\rho(n) = R_n - R_r$, can be calculated from the same geometric relationship shown in Figure 2. Here, $\rho(n)$ corresponds to the path difference Δd_n in Figure 2, but the reference point is changed from element 1 to the positioning antenna. Let $\mathbf{b}_n$ be the baseline vector from the positioning antenna to element n, and let $L = \|\mathbf{b}_n\|$. Therefore, the path difference is obtained as the projection of $\mathbf{b}_n$ onto the incident direction of the GNSS signal:

$$\rho(n) = R_n - R_r \approx -\mathbf{b}_n^T \mathbf{u}(\theta, \varphi) = L\cos\alpha \tag{10}$$

The integer carrier-phase ambiguity term does not affect the final beam pointing. Only the phase offset within one wavelength is of interest. After rearranging the terms, we obtain $\Delta\varphi_n$, namely the phase difference between array element n and the positioning antenna:

$$\Delta\varphi_n = (\varphi_n - \varphi_r) = -\left[\Delta\Phi_n + \frac{2\pi}{\lambda}\rho(n) + (\varepsilon_n - \varepsilon_r)\right] \tag{11}$$

Here, $\Delta\Phi_n$ is measured and $\rho(n)$ is known. The residual noise term mainly comes from the thermal noise of the carrier-tracking phase-locked loop (PLL) in the GNSS receiver [26]. Its effect on the calibration result will be discussed in Section 3 and is neglected here.

To eliminate the delay of the positioning antenna φ_r, a second differencing operation is performed. Under typical conditions, full-array calibration of a 6×6 spaceborne phased array can be completed within 10 min. During this period, the thermal control system can maintain a relatively constant device temperature, so φ_r can be treated as constant. Taking the single-difference result of element 1 as reference, the second difference for any element n is

$$\nabla\Delta\varphi_n = (\varphi_n - \varphi_r) - (\varphi_1 - \varphi_r) = \varphi_n - \varphi_1 \tag{12}$$

The total phase delay φ_n contains three terms, among which $\varphi_{o,k}$ is the receiver channel delay after the beamforming network. If k beams need to be synthesized, the receiver has k backend channels, and any one of them can be used for calibration. With all output signals from the beamforming network routed through the same channel, the $\varphi_{o,k}$ can be eliminated. Since the phase shifters are set to zero, the second difference becomes (assume channel 1 is selected for reception)

$$\begin{aligned} \nabla\Delta\varphi_n &= (\varphi_{e,n} + \varphi_{d,n} + \varphi_{o,k}) - (\varphi_{e,1} + \varphi_{d,1} + \varphi_{o,1}) \\ &= (\varphi_{e,n} + 0 + \varphi_{o,1}) - (\varphi_{e,1} + 0 + \varphi_{o,1}) \\ &= \varphi_{e,n} - \varphi_{e,1} = \Delta\varphi_{e,n} \end{aligned} \tag{13}$$

Thus, the relative additional phase error of element n with respect to element 1 is isolated successfully. The microwave switch matrix subsequently switches to the next element, and the same procedure is repeated until the entire array is calibrated. The overall calibration procedure is illustrated in Figure 6.

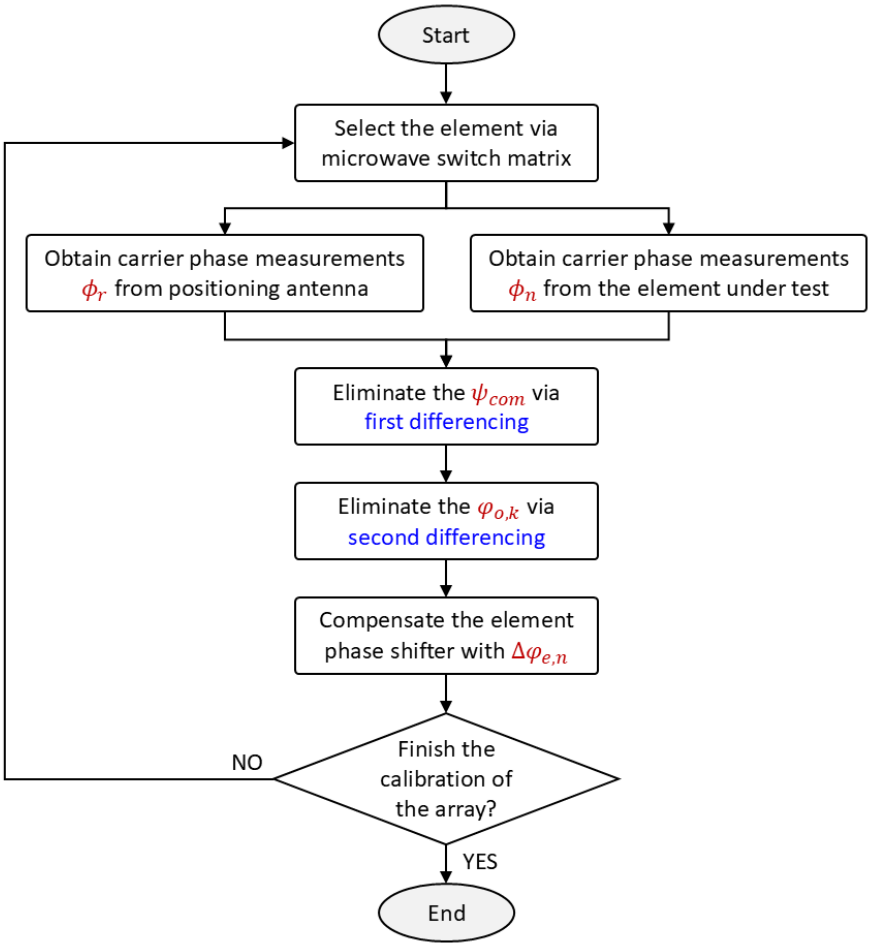


Figure 6. Flowchart of the calibration process.

3. Results

To further verify the accuracy of the proposed method, a Monte Carlo simulation is conducted in this section. It should be emphasized that the calibration objective of this work is not full-aperture far-field electromagnetic calibration, but rather the estimation of the relative receive-chain phase error of the selected array element with respect to the reference element. Therefore, the embedded element phase, PCV, mutual coupling, and residual phase errors caused by the installation are considered as residual errors after pre-launch ground calibration.

The double-difference calibration residual of the n-th array element can be written as

$$\varepsilon_n = \varepsilon_{\mathrm{PLL},n} + \varepsilon_{\mathrm{geo},n} + \varepsilon_{\mathrm{ref},n} + \varepsilon_{\mathrm{mp},n} + \varepsilon_{\mathrm{sw},n} + \varepsilon_{\mathrm{time},n} + \varepsilon_{\mathrm{com},n} \tag{14}$$

where the definitions of the error terms are summarized in Table 3.

Cycle slips or phase resets are handled through carrier-tracking quality control and are not included as regular error terms in the nominal simulation.

The thermal noise of the carrier tracking loop is calculated using the Costas-loop model. For a given carrier-to-noise density ratio C/N_0, the relationship is expressed as

$$\sigma_{\mathrm{PLL}} = \frac{\lambda}{2\pi}\sqrt{\frac{B_L}{C/N_0}\left(1+\frac{1}{2TC/N_0}\right)} \tag{15}$$

where λ is the wavelength of the GPS L1 carrier, B_L is the loop noise bandwidth, and T is the predetection integration time. Unlike the previous simplified analysis, this section

does not assume an identical fixed C/N_0 for all array elements. Instead, a stochastic link-budget model is established. The effective carrier-to-noise density ratios of the selected array element receiving path and the positioning antenna receiving path are calculated separately as

$$(C/N_0)_i = EIRP_{\text{eff}} + G_i - L_{\text{FS}} - L_{\text{RF},i} - L_{\text{pol},i} - L_{\text{blk},i} - (-174 + NF_i) \quad (16)$$

where the definitions of the link-budget terms are summarized in Table 4.

Table 3. Definition of error terms in the calibration residual model.

Error Term	Description
$\varepsilon_{\text{PLL},n}$	Carrier tracking-loop thermal noise, mainly determined by C/N_0, loop bandwidth, and integration time.
$\varepsilon_{\text{geo},n}$	Geometric projection residual caused by relative element position error and attitude error.
$\varepsilon_{\text{ref},n}$	Antenna phase-reference residual, including phase center variation, embedded element response, and installation-environment residuals.
$\varepsilon_{\text{mp},n}$	Multipath residual caused by reflected or scattered GNSS signals.
$\varepsilon_{\text{sw},n}$	Microwave-switch phase repeatability error during sequential element selection.
$\varepsilon_{\text{time},n}$	Receive-chain temporal drift caused by non-strictly synchronous observations.
$\varepsilon_{\text{com},n}$	Residual common-mode error not fully cancelled over a short observation interval.

Table 4. Definition of terms in the stochastic link-budget model.

Term	Description
$EIRP_{\text{eff}}$	Effective GNSS equivalent isotropically radiated power, accounting for both GNSS transmit-power fluctuation and transmitting antenna pattern variation.
G_i	Receiving antenna gain of the i-th receiving path.
L_{FS}	Free-space propagation loss between the GNSS satellite and the LEO satellite platform.
$L_{\text{RF},i}$	RF-chain loss of the i-th receiving path, including losses introduced by switches, cables, and RF components.
$L_{\text{pol},i}$	Polarization mismatch loss of the i-th receiving path.
$L_{\text{blk},i}$	Blockage or installation-environment loss of the i-th receiving path.
NF_i	Noise figure of the i-th receiving chain.

The simulation adopts a 6×6 uniform planar array with an element spacing of 0.5λ. The carrier frequency is GPS L1, and the wavelength is approximately 190.3 mm. The incident direction of the GNSS signal is set to an elevation angle of 45° and an azimuth angle of 30°. The main Monte Carlo simulation contains 1200 trials. In the nominal link-budget setting, the mean effective GNSS EIRP is set to 55 dBm, and the mean free-space path loss is set to 187 dB. For the selected array element path, the mean element gain is set to 4 dBi, the mean RF-chain loss is set to 2 dB, and the noise figure is set to 2 dB. For the positioning antenna path, the mean antenna gain is set to 3 dBi, the mean RF-chain loss is set to 1.5 dB, and the noise figure is also set to 2.5 dB. For the geometric error terms, the standard deviation of the relative element position residual is set to 0.5 mm, and the standard deviation of the attitude error is set to 0.1°. The PCV/embedded element phase-reference residual is set to 0.5 mm, the multipath residual is set to 0.5 mm, and the standard deviation of the switch phase repeatability error is set to 0.5 mm.

A fast interleaved sampling strategy is adopted for the reference element, where the reference element is rapidly re-observed before or after the observation of the element under testing. The tracking time for each selected state is set to 5 s, and the switching overhead is set to 0.2 s. Under this setting, the total time required to complete the relative phase calibration of the 6×6 array is approximately 6 min.

Figure 7 shows the calibration error distribution under the nominal stochastic link-budget. The simulation results indicate that the calibration error approximately follows a zero-mean distribution. The overall RMS error is 3.02 mm, corresponding to a phase error of approximately 5.72° at the GPS L1 frequency. This value is close to the minimum phase step of a 6-bit digital phase shifter, namely 5.625°. Under higher C/N_0 conditions and with well-controlled geometric and phase-reference residuals, the calibration accuracy can be further improved.

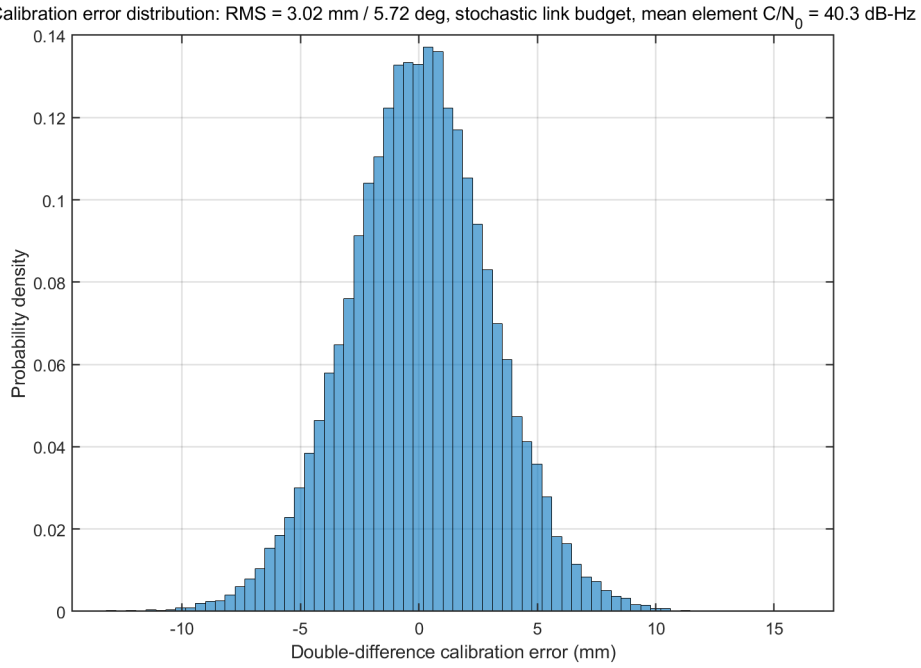


Figure 7. Calibration error distribution under the nominal stochastic link-budget model. The RMS calibration error is 3.02 mm, corresponding to 5.72° at the GPS L1 frequency, with a mean element path C/N_0 of 40.3 dB-Hz.

To further illustrate the influence of the calibration residual on array beam performance, Figure 8 presents the beam-level validation results under different C/N_0 conditions. When $C/N_0 = 30$ dB-Hz, the calibration residual RMS is approximately 16.6° due to the relatively large carrier-tracking noise, and noticeable sidelobe deviations remain in the pattern. When $C/N_0 = 40$ dB-Hz, the calibration residual RMS decreases to approximately 5.6°, and the main-lobe region and first-sidelobe region become close to those of the ideal pattern.

Figure 9 further presents the sensitivity analysis of key parameters. First, the calibration accuracy is most sensitive to C/N_0. When the fixed C/N_0 increases from 30 dB-Hz to 46 dB-Hz, the RMS error decreases from 8.8 mm to approximately 1.8 mm. This indicates that C/N_0 is the key factor determining the upper limit of calibration accuracy.

Second, the geometric projection residual has a moderate influence on the result. When the element position error and attitude error are increased proportionally, the RMS error rises from approximately 2.9 mm to approximately 3.5 mm.

By contrast, after adopting the fast interleaved sampling strategy for the reference element, the time interval between the reference element and the element under test has

only a minor influence on the total error. This demonstrates that the proposed strategy can effectively suppress the temporal drift error caused by the non-synchronism of the second difference. When the PCV/embedded element response residual and the multipath residual vary within the range of 0–0.5 mm, the total RMS error remains approximately around 3 mm. This indicates that, under controlled residual error conditions, these two error sources do not become the dominant limiting factors. When the mean RF-chain loss increases from 0.5 dB to 2.0 dB, the RMS error increases only slightly, indicating that RF loss mainly affects the calibration accuracy indirectly by reducing C/N_0.

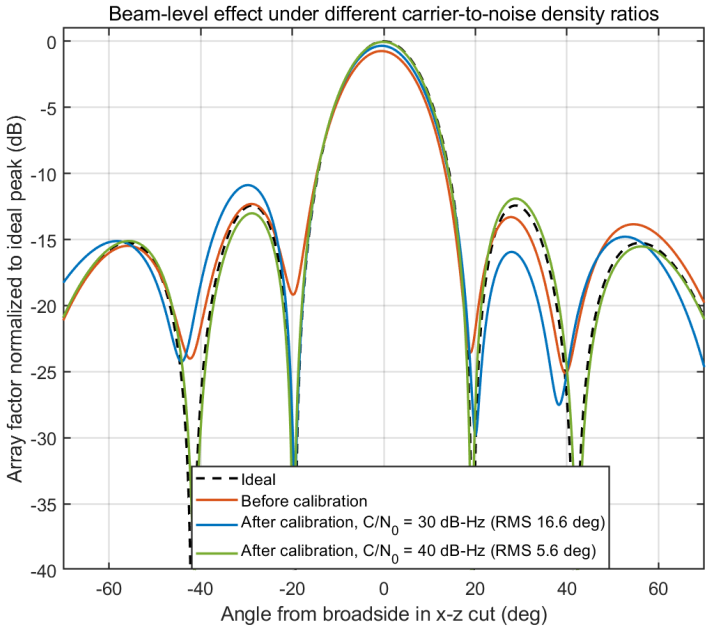


Figure 8. Beam-level validation under different carrier-to-noise density ratios. The ideal pattern, the uncalibrated pattern, and the calibrated patterns under $C/N_0 = 30$ dB-Hz and $C/N_0 = 40$ dB-Hz are compared to evaluate the effect of calibration residuals on the array radiation pattern.

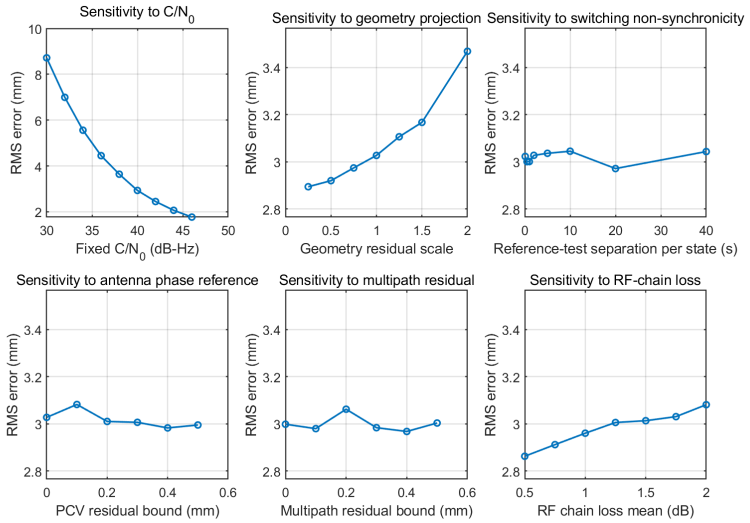


Figure 9. Sensitivity analysis of the calibration accuracy. The RMS calibration error is evaluated with respect to the carrier-to-noise density ratio, geometry projection residual, switching non-synchronicity, antenna phase-reference residual, multipath residual, and RF-chain loss.

In summary, the proposed method can achieve an RMS error of approximately 3.02 mm under typical operating conditions, corresponding to a GPS L1 phase error of approximately 5.72°. Without relying on a dedicated transmitting excitation source, the

proposed method avoids self-interference in the GNSS frequency band while achieving a relative phase calibration accuracy close to the minimum phase step of a 6-bit phase shifter. Therefore, it provides a valuable reference for in-orbit phase-drift monitoring and auxiliary calibration of phased array receive chains.

4. Conclusions

This article presents a passive double-difference calibration algorithm for phased array antennas in orbit. By exploiting the short-baseline property between the positioning antenna and the element under test, together with a shared high-stability clock, the first differencing operation suppresses common-mode errors such as ionospheric delay, tropospheric delay, and receiver clock bias. By further exploiting receiver channel consistency, the second differencing operation reduces the influence of receiver channel delay and supports the estimation of the relative receive-chain phase errors of the selected array elements. A stochastic link-budget model and a residual error budget are introduced to evaluate the calibration accuracy under more realistic operating conditions. The simulation results show that, under typical conditions, the proposed method achieves an RMS calibration error of approximately 3.02 mm, corresponding to a phase error of approximately 5.72° at the GPS L1 frequency. This accuracy is close to the 5.625° minimum phase step of a 6-bit digital phase shifter, and can be further improved under higher-C/N_0 and well-controlled residual error conditions.

The proposed method does not require an additional GNSS band calibration signal. It therefore avoids introducing a dedicated co-frequency excitation source near the positioning antenna during calibration. The method has a clear formulation and uses visible GNSS satellites as passive radiation sources, providing an auxiliary technical approach for in-orbit phase-drift monitoring and relative receive-chain phase calibration of phased array antennas on LEO satellites. Future work will further validate the method through hardware-in-the-loop experiments or in-orbit measurement data, and will investigate the influence of embedded element responses, platform scattering, phase center variation, and scan-angle dependence when extending the method toward more complete aperture-level calibration.

Author Contributions: Conceptualization, Q.D., Z.W., Y.S. and X.M.; methodology, Q.D., Z.W., Y.S. and X.M.; software, Z.W.; validation, Q.D., Z.W., Y.S. and X.M.; investigation, J.X., D.W. and H.Z.; writing—original draft preparation, Q.D. and Z.W.; writing—review and editing, Q.D., Z.W., Y.S. and X.M.; visualization, Q.D., Z.W., Y.S. and X.M.; supervision, Q.D., Y.S. and X.M. All authors have read and agreed to the published version of the manuscript.

Funding: This research received no external funding.

Data Availability Statement: Data are contained within the article.

Conflicts of Interest: The authors declare no conflicts of interest.

References

1. Han, Y.; Ying, T.; Yang, J.; Zhao, Y.; Li, X. Optimization of Radiation Shielding Composite Materials Tailored for Space Mission Applications. *IEEE Trans. Nucl. Sci.* **2025**, *72*, 1790–1799. [CrossRef]
2. Brunetti, G.; Campiti, G.; Tagliente, M.; Ciminelli, C. COTS Devices for Space Missions in LEO. *IEEE Access* **2024**, *12*, 76478–76514. [CrossRef]
3. Kaschmitter, J.; Shaeffer, D.; Colella, N.; McKnett, C.; Coakley, P. Operation of commercial R3000 processors in the Low Earth Orbit (LEO) space environment. *IEEE Trans. Nucl. Sci.* **1991**, *38*, 1415–1420. [CrossRef]
4. Gutiérrez, O.; Prieto, M.; Perales-Eceiza, A.; Ravanbakhsh, A.; Basile, M.; Guzmán, D. Toward the Use of Electronic Commercial Off-the-Shelf Devices in Space: Assessment of the True Radiation Environment in Low Earth Orbit (LEO). *Electronics* **2023**, *12*, 4058. [CrossRef]

5. Yoon, H.J.; Min, B.W. Improved Rotating-Element Electric-Field Vector Method for Fast Far-Field Phased Array Calibration. *IEEE Trans. Antennas Propag.* **2021**, *69*, 8021–8026. [CrossRef]
6. Sarayloo, Z.; Masoumi, N.; Nezhadahmadi, M.R.; Ahmadabadi, M.N. Fourier-Gated Transformer and MLP-Enhanced REV: Noise-Robust Phased-Array Antenna Calibration Using Power-Only Measurements. *IEEE Trans. Instrum. Meas.* **2026**, *75*, 2505224. [CrossRef]
7. Fan, W.; Zhang, Y.; Wang, Z.; Zhang, F. Large-Scale Phased Array Calibration Based on Amplitude-Only Measurement with the Multiround Grouped-REV Method. *IEEE Trans. Antennas Propag.* **2024**, *72*, 454–465. [CrossRef]
8. Silverstein, S. Application of orthogonal codes to the calibration of active phased array antennas for communication satellites. *IEEE Trans. Signal Process.* **1997**, *45*, 206–218. [CrossRef] [PubMed]
9. Muin, F.; Hariyadi, T.; Park, J.W.; Kong, S.; Kim, P.; Park, S.O. Compact K-Band Phased Array Antenna with Orthogonal Calibration and Error Assessment. *IEEE Access* **2025**, *13*, 163258–163275. [CrossRef]
10. Lier, E.; Zemlyansky, M.; Purdy, D.; Farina, D. Phased array calibration and characterization based on orthogonal coding: Theory and experimental validation. In Proceedings of the 2010 IEEE International Symposium on Phased Array Systems and Technology, Waltham, MA, USA, 12–15 October 2010; pp. 271–278. [CrossRef]
11. Wang, B.; Tian, B.; Li, Y. Review of calibration techniques for space-borne active array antenna. In Proceedings of the 2016 Progress in Electromagnetic Research Symposium (PIERS), Shanghai, China, 8–11 August 2016; p. 2778. [CrossRef]
12. Liang, W.; Jia, Z.; Hong, J.; Zhang, Q.; Wang, A.; Deng, Z. Polarimetric Calibration Scheme Combining Internal and External Calibrations, and Experiment for Gaofen-3. *IEEE Access* **2020**, *8*, 7659–7671. [CrossRef]
13. Jiao, Y.; Liu, K.; Yue, H.; Zhang, H.; Zhao, F. An Innovative Internal Calibration Strategy and Implementation for LT-1 Bistatic Spaceborne SAR. *Remote Sens.* **2024**, *16*, 2965. [CrossRef]
14. Jiao, Y.; Wu, L.; Ai, Z.; Zheng, M.; Zhang, H.; Zhao, F. An Advanced Real-Time Internal Calibration Scheme for the DBF-SCORE Spaceborne SAR Systems. *Remote Sens.* **2025**, *17*, 1425. [CrossRef]
15. Makhoul, E.; Broquetas, A.; Lopez-Dekker, F.; Closa, J.; Saameno, P. Evaluation of the Internal Calibration Methodologies for Spaceborne Synthetic Aperture Radars with Active Phased Array Antennas. *IEEE J. Sel. Top. Appl. Earth Obs. Remote Sens.* **2012**, *5*, 909–918. [CrossRef]
16. Anantharamu, P.B.; Borio, D.; Lachapelle, G. Self-Contained Antenna Array Calibration using GNSS Signals. *Navigation* **2012**, *59*, 209–220. [CrossRef]
17. Schuss, J.J.; Sikina, T.V.; Hilliard, J.E.; Makridakis, P.J.; Upton, J.; Yeh, J.C.; Sparagna, S.M. Large-Scale Phased Array Calibration. *IEEE Trans. Antennas Propag.* **2019**, *67*, 5919–5933. [CrossRef]
18. Schuss, J.; Sikina, T.; Hilliard, J.; Makridakis, P.; Upton, J.; Yeh, J.; Sparagna, S. Large Scale Phased Array Calibration Using Satellites. In Proceedings of the 2019 IEEE International Symposium on Phased Array System and Technology (PAST), Waltham, MA, USA, 15–18 October 2019; pp. 1–5. [CrossRef]
19. Wang, T.; Ruf, C.S.; O'Brien, A.J.; Gleason, S.; McKague, D.S.; Block, B.P.; Russel, A. Measurement of GPS Antenna Gain Patterns for CYGNSS Using a Spaceborne Antenna Range. *IEEE Trans. Aerosp. Electron. Syst.* **2024**, *60*, 6883–6893. [CrossRef]
20. Zhang, H.; Xu, Y.; Luo, R.; Mao, Y. Fast GNSS acquisition algorithm based on SFFT with high noise immunity. *China Commun.* **2023**, *20*, 70–83. [CrossRef]
21. Li, J.; Sun, R.; Wang, Y.; Ochieng, W.Y. A robust time synchronization algorithm for GNSS/IMU integrated navigation in urban environments. *Meas. Sci. Technol.* **2025**, *36*, 036302. [CrossRef]
22. Zhang, Y.; Shen, Y.; Soh, Y.C.; Niu, W.; Xue, F.; Wang, H.; Liu, W. Directionally Regularized Two-Stage Calibration for Cross-Shaped MGT Sensor Arrays with Physics-Inspired Error Modeling. *IEEE Trans. Instrum. Meas.* **2026**, *75*, 9508112. [CrossRef]
23. Zhang, X.F. *Array Signal Processing and MATLAB Implementation*, 3rd ed.; Publishing House of Electronics Industry: Beijing, China, 2023.
24. Gao, T.; Jin, X.; Wang, L. An array antenna calibration method based on GNSS signal. In Proceedings of the 2018 12th International Symposium on Antennas, Propagation and EM Theory (ISAPE), Hangzhou, China, 3–6 December 2018; pp. 1–4. [CrossRef]
25. Kurganov, V.V. Antenna Array Complex Channel Gain Estimation Using Phase Modulators. In Proceedings of the 2019 Antennas Design and Measurement International Conference (ADMInC), St. Petersburg, Russia, 16–18 October 2019; pp. 126–129. [CrossRef]
26. Kaplan, E.D.; Hegarty, C. *Understanding GPS/GNSS: Principles and Applications*; Artech House: New York, NY, USA, 2017.

Disclaimer/Publisher's Note: The statements, opinions and data contained in all publications are solely those of the individual author(s) and contributor(s) and not of MDPI and/or the editor(s). MDPI and/or the editor(s) disclaim responsibility for any injury to people or property resulting from any ideas, methods, instructions or products referred to in the content.